High-Precision Detection Method for Structure Parameters of Catenary Cantilever Devices Using 3-D Point Cloud Data

Wenqiang Liu, *Graduate Student Member, IEEE*, Zhigang Liu, *Senior Member, IEEE*, Qiao Li, *Graduate Student Member, IEEE*, Zhiwei Han, *Member, IEEE*, and Alfredo Núñez, *Senior Member, IEEE*

***Abstract*— This article proposes an automatic high-precision detection method for structure parameters of catenary cantilever devices (SPCCDs) using 3-D point cloud data. The steps of the proposed detection method are: 1) segmenting and recognizing the components of the catenary cantilever devices, 2) extracting the detection plane and backbone component axis of catenary cantilever devices, and 3) detecting the SPCCD. The effective segmentation of components is critical for structure parameter detection. A point cloud segmentation and recognition method based on three-dimensional convolutional neural networks (3-D CNNs) is introduced to determine the different components of the catenary cantilever devices. Compared with traditional unsupervised clustering procedures for point cloud segmentation, the proposed method can improve the segmentation accuracy, does not require complex tuning procedures of parameters, and improves robustness and stability. Additionally, the segmentation method defines a recognition function, facilitating the analysis of the structural relationship between objects. Furthermore, we proposed an improved projection random sample consensus (RANSAC) method, which can effectively divide the detection plane of catenary cantilever devices to solve the multicantilever device occlusion problem. With RANSAC, it is also possible to precisely extract the backbone component axis and enhance parameter detection accuracy. The experimental results show that the structure angle and steady arm slope's error accuracy can achieve 0.1029° and 1.19%, respectively, which indicates the proposed approach can precisely detect the SPCCD.**

***Index Terms*— Catenary cantilever devices, point cloud segmentation, random sample consensus (RANSAC), structure parameter detection, three-dimensional convolutional neural networks (3-D CNNs).**

Manuscript received October 17, 2020; revised November 27, 2020; accepted December 7, 2020. Date of publication December 18, 2020; date of current version January 8, 2021. This work was supported in part by the National Natural Science Foundation of China under Grant 51977182 and Grant U1734202. The Associate Editor coordinating the review process was Dr. Octavian Adrian Postolache. *(Corresponding author: Zhigang Liu.)*

Wenqiang Liu, Zhigang Liu, Qiao Li, and Zhiwei Han are with the School of Electrical Engineering, Southwest Jiaotong University, Chengdu 610031, China (e-mail: liuwq_2009@126.com; liuzg_cd@126.com; 747049448@qq.com; zw.han@my.swjtu.edu.cn).

Alfredo Núñez is with the Section of Railway Engineering, Department of Engineering Structures, Delft University of Technology, 2628 CN Delft, The Netherlands (e-mail: a.a.nunezvicencio@tudelft.nl).

Digital Object Identifier 10.1109/TIM.2020.3045801

NOMENCLATURE

SPCCD	Structure parameters of catenary cantilever devices.
3-D CNNs	Three-dimensional convolutional neural networks.
RANSAC	Random sample consensus.
PSO-GAPF	Genetic particle filter algorithm based on particle swarm optimization.
SC_LCCP	Slope constrained locally convex connected patches.
SVC	Super-voxel clustering.
LCCP	Locally convex connected patches.
IP_RANSAC	Improved projection random sample consensus.
3-D PointCNN	Three-dimensional point convolutional neural network.
MLP	Multilayer perceptron.
FPS	Farthest point sampling.
RTX	Real time exchange.
GPU	Graphics processing unit.
RAM	Random access memory.
SSD	Solid state disk.

I. INTRODUCTION

AS A support device for fixing the catenary component, the catenary cantilever device is vital to the traction power supply system in high-speed railway systems [1]. As shown in Fig. 1, the contact wire is attached and fixed in the positioning clamp of catenary cantilever devices.

When a train runs, the pantograph collects the current from the contact wire to supply the train. To guarantee the current collection quality and to allow vehicles to run smoothly and safely, it is vital to monitor the stability of the catenary cantilever device structure periodically [2], [3]. With the rapid development of artificial intelligence technologies, advanced vision-based noncontact detection methods for component failures [4]–[10] and structure parameters measurement [11]–[14] of the catenary are proposed in the literature.

Detection methods using 2-D images mainly focus on spatial structure parameters of components. For example,

1557-9662 © 2020 IEEE. Personal use is permitted, but republication/redistribution requires IEEE permission.
See https://www.ieee.org/publications/rights/index.html for more information.

Authorized licensed use limited to: TU Delft Library. Downloaded on January 13,2021 at 10:26:00 UTC from IEEE Xplore. Restrictions apply.

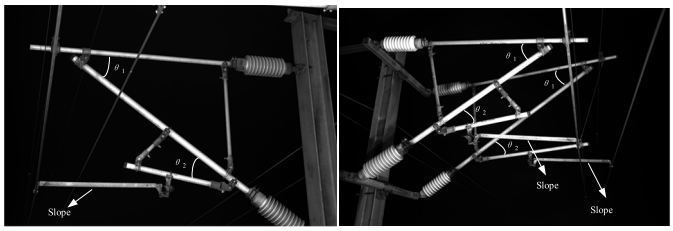

(a) (b)

Fig. 1. Two-dimensional image of catenary cantilevers: (a) in normal catenary regions and (b) in catenary transition regions.

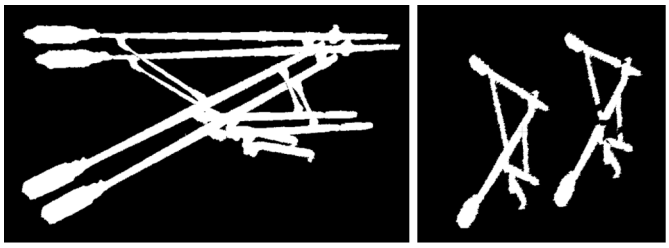

(a) (b)

Fig. 2. Three-dimensional point cloud of catenary cantilevers: (a) front view and (b) oblique view.

Cho and Ko [11] proposed a video-based dynamic stagger measurement of railway overhead power contact wires. The rotation-invariant feature matching is used to detect and locate the pantograph. According to the edge intersection point of the contact wire and the pantograph, the stagger value is detected. Liu *et al.* [12] presented a conductor height and stagger measurement using laser imaging and visual tracking. First, a beam of fan laser hits the contact wire to form a target spot. Then, the spot is tracked with the PSO-GAPF algorithm. Lastly, according to space coordinate transformation, the geometric parameters are obtained. Zhan *et al.* [13] proposed a vision-based detection approach for railway catenary geometry parameters. They used a binocular vision component composed of two line-scan cameras to calculate the space intersection point, and then the parameters were obtained according to the triangulation measurement principle. Yang *et al.* [14] proposed a parameter detection method for the steady arm slope of catenary cantilever devices. First, the steady arm was located and extracted by combining the CNN-based rough detection and the Hough transformation-based fine detection. The steady arm slope was then measured by calculating its spatial coordinates using a novel monocular vision model.

The 2-D images-based methods discussed mainly focus on the parameter detection for simple environments, such as the geometric parameter of catenary suspension devices and the steady arm slope parameter of catenary cantilever devices. The detection of these parameters is not susceptible to background interference and is, in general, evaluated under simple conditions, especially the catenary suspension devices [11]–[14]. However, for the detection of the SPCCDs, as shown in Fig. 1(a), the methods do not provide a high-precision estimation, particularly, in cases with a complex background in the transition regions, as shown in Fig. 1(b). A possible solution to capture the devices' spatial information and to detect these structure parameters more precisely is to consider 3-D depth information (as shown in Fig. 2). With the development of driverless technology, nowadays, it is possible to update 3-D data collection equipment and 3-D detection technology based on artificial intelligence. These data sources make it possible to increase the level of details about the condition of the railway infrastructure obtained during inspection programs. The literature so far of 3-D point cloud data for railway applications is somewhat limited [15]–[18]. Han *et al.* [19] used 3-D point cloud data to detect the SPCCDs, as shown in Fig. 3. The proposed method uses a traditional unsupervised clustering segmentation procedure. The technique, abbreviated as SC_LCCPs, combined the SVC [20] and the LCCPs [21] to segment the components of catenary cantilever devices. After that, a line detection with an RANSAC method [22] was used for the segmented regions to calculate catenary cantilevers' structure parameters. The method can be further improved when considering the following aspects.

1) The unsupervised clustering method for point cloud segmentation SC_LCCP was considered [see Fig. 3(b)]. A significant problem of the method is that it requires setting and adjusting manually various model parameters. Complicated tuning procedures are needed, as low robustness of the model is obtained when considering preadjusted parameters. Besides, to calculate the structure parameters, the category of each segmented component should be determined first. However, SC_LCCP is an unsupervised clustering method that cannot identify components. Therefore, they use the prior relationship of the structure of catenary cantilever devices to determine the component category. However, due to adjustments of catenary cantilever devices during on-site installation and during operations, the assumed prior relationship would contain a degree of uncertainty, which will affect the accuracy of the component category identification.
2) The method was evaluated considering a simple structure in typical catenary regions, as shown in Fig. 1(a). A method designed to address challenging cases, such as the occlusion situation shown in Fig. 1(b) that the 2-D image method can solve in the transition regions, is still needed in the literature.
3) Lastly, the projection RANSAC straight-line detection method was proposed to extract the backbone component axis of catenary cantilever devices to measure the structure parameters. As shown in Fig. 3(c), point clouds are first projected to X–O–Y plane, and these straight lines are detected, which ignores the spatial relationships in the Z dimension. In Fig. 3(c), the point N' deviates from the detection plane, although they are still on the same line in the projection plane. When the points M'N' are mapped back, it may lead that the line MN is detected, and the result will face a slight deviation when calculating the angle.

To solve the above problems, we proposed a novel detection method for SPCCD using 3-D CNNs and the

Authorized licensed use limited to: TU Delft Library. Downloaded on January 13,2021 at 10:26:00 UTC from IEEE Xplore. Restrictions apply.

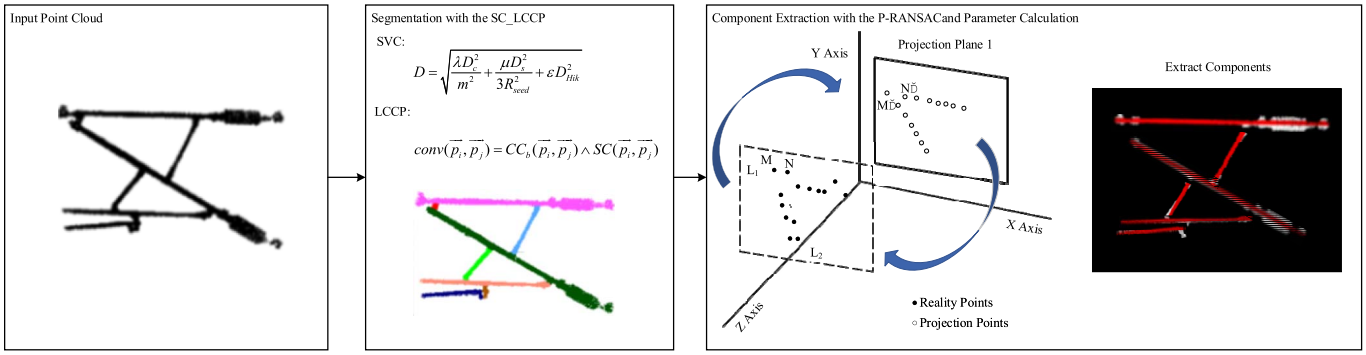

Fig. 3. Pipeline of the SPCCD detection system using the traditional SC_LCCP [19]. (a) Input point cloud. (b) Segmentation with SC_LCCP. (c) Component extraction with RANSAC and parameter calculation.

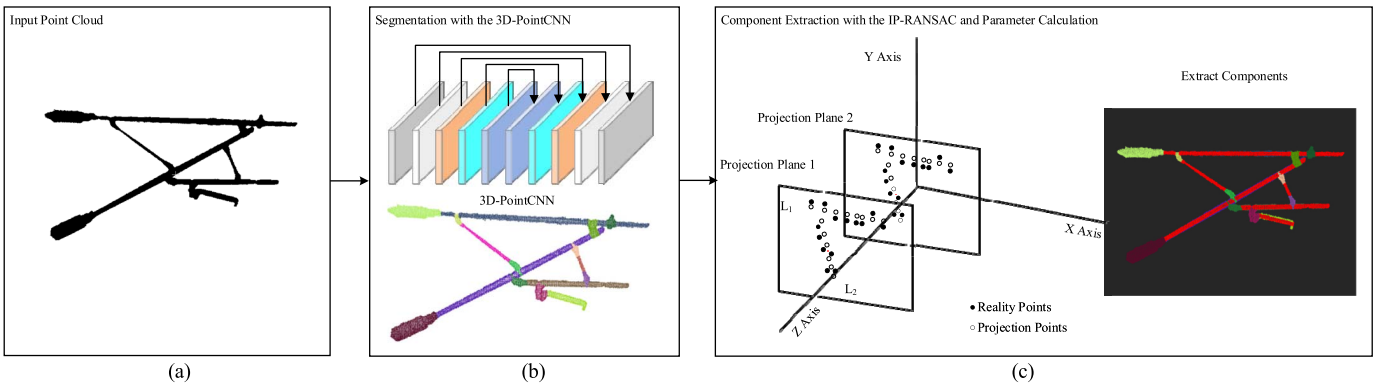

Fig. 4. Pipeline of the proposed SPCCD detection method using 3-D CNN. (a) Input point cloud. (b) Segmentation with 3-D PointCNN. (c) Component extraction with IP-RANSAC and parameter calculation.

RANSAC method. The proposed method is shown in Fig. 4. The contributions of this article are summarized as follows:

1) For the component segmentation, a model based on 3-D CNNs is introduced to segment catenary cantilevers, as shown in Fig. 4(b). Compared with the unsupervised clustering SC_LCCP, there are two advantages: 1) an extensive 3-D point cloud data set is used to train a neural network, avoiding manual parameter setting and adjustment and 2) as a supervised method, it can accurately recognize components, and it is not dependent on prior information about the relationship between the elements of the catenary cantilever devices.
2) For the SPCCD calculation, we propose an improved projection RANSAC (IP_RANSAC) method, as shown in Fig. 4(c). First, the spatial characteristics from 3-D point cloud data are fully used. A fast plane detection method is proposed to divide multicantilever devices and solve the occlusion problem in transition regions. Then, point cloud data are projected to the detected plane, and the backbone component axis is extracted from the projected plane. The parameter calculation can be directly performed from the extracted component axis in the projected plane. This can avoid the problem in [19] when the point cloud data are mapped back to the original space, and it can improve the measurement accuracy of the detected SPCCD.

This article is organized as follows. Section II introduces the segmentation model based on 3-D CNNs. The proposed structure parameters detection method based on RANSAC is explained in Section III. Experimental results are analyzed and discussed in Section IV. The conclusions of this work are summarized in Section V.

II. Catenary Cantilever Segmentation

We introduce an advanced recognition and segmentation model based on 3-D CNNs to improve the traditional methods' segmentation accuracy. The goal is to enhance the detection precision of SPCCD. Section II-A describes the recognition and segmentation networks.

A. 3-D Point Convolutional Neural Networks

In the literature, CNNs are widely used to learn hierarchical feature representations through leveraging the spatially local correlation in image-pixels 2-D regular grids, as illustrated in the upper part of Fig. 5 [23]. Extensions of CNNs based on hierarchical architectures have been applied to higher dimensional regular domains. However, 3-D point cloud data are in a disordered and irregular domain, as shown in the lower part of Fig. 5. It is not straightforward to directly utilize the extended CNNs to extract 3-D point cloud data features. With the rapid advances and large demands of 3-D sensing technologies, especially from the driverless vehicles industry, some recent feature learning developments from 3-D point cloud data have been presented [24]–[33]. These methods have different advantages and disadvantages. For example, the authors of [24]–[28] successfully

Authorized licensed use limited to: TU Delft Library. Downloaded on January 13,2021 at 10:26:00 UTC from IEEE Xplore. Restrictions apply.

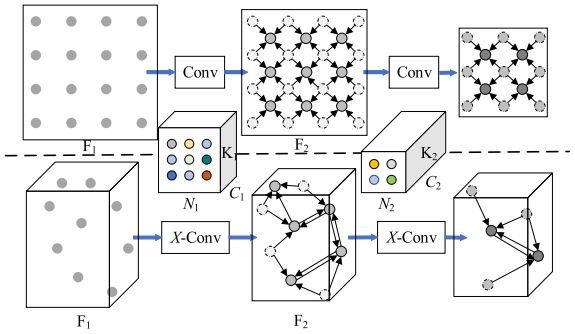

Fig. 5. Hierarchical convolution on regular grids and point clouds.

achieved order invariance, but they lost valuable information. In [29]–[33], these methods can apply typical CNNs through "interpolate" or "project" features into predefined regular domains. However, the kernels associated with each point were individually parametrized, and they are insufficient to extract the local structures. For these above problems, Li *et al.* [34] proposed a general and straightforward framework called 3-D PointCNN. The framework exploits the advantages of CNNs to learn the features directly from 3-D point cloud data. The idea of the 3-D PointCNN is that K candidate points $(p_1, p_2, \ldots, p_k)$ are selected from the previous layer. Then, a KK transformation matrix (named X-transformation) is learned through the use of the MLP, which is $X = \text{MLP}(p_1, p_2, \ldots, p_k)$. The matrix is used to perform the weighting and permutation for input features. After that, the transformed features can be processed with conventional CNNs. The entire process is called X-Conv operator. The architecture diagram based on the X-Conv operator is shown in Fig. 6. The X-Conv operator is described next.

1) X-Conv Operator:

Step 1 (Point "Projected"): First, the farthest point sampling (FPS) is utilized to reduce the number of samples $\mathrm{F}_1 = \{(p_{1,i}, f_{1,i}): i = 1, 2, \ldots, N_1, p_{1,i} \in R^{\mathrm{Dim}}\}$, each associated with a feature $\{f_{1,i}: f_{1,i} \in R^{C_1}\}$ and choose the representative points $\mathrm{F}_2 = \{(p_{2,i}, f_{2,i}): j = 1, 2, \ldots, N_2\}$ from the set $(p_{1,i})$ by the FPS, which are the points that are beneficial to the information "projection," and now the feature dimensional of F_2 is C_1, so $f_{2,i} \in R^{C_1}$. Then, K nearest neighbor points $\boldsymbol{P}$ $(p_1, p_2, \ldots, p_k, p \in R^{K \times \mathrm{Dim}})$ of each representative point $(p_{2,j})$ in the previous layer are projected into the local coordinate system centered on each representative point. Among, N represents the number of points, and C denotes the channels, $N_1 > N_2$ and $C_1 < C_2$

$$\boldsymbol{P}' = \boldsymbol{P} - p_{2,j}. \tag{1}$$

Step 2 (Lift Dimensional Space): The $\boldsymbol{P}$ sets of each point in p are mapped and lifted into a $C_{.\delta}$ dimensional space through $\mathrm{MPL}_{.\delta}$, and then a new feature of each representative point $(p_{2,j})$ is obtained, $\boldsymbol{f}^{\delta}_{2,j} \in R^{k \times C_\delta}$

$$\boldsymbol{f}^{\delta}_{2,j} = MLP_{\delta}(\boldsymbol{P}'). \tag{2}$$

Step 3 (Concatenate Feature): Then, the features $\boldsymbol{f}^{\delta}_{2,j}$ and $\boldsymbol{f}_{2,j}$ are concatenated together, forming a new feature $\boldsymbol{f}_{2,j}$,

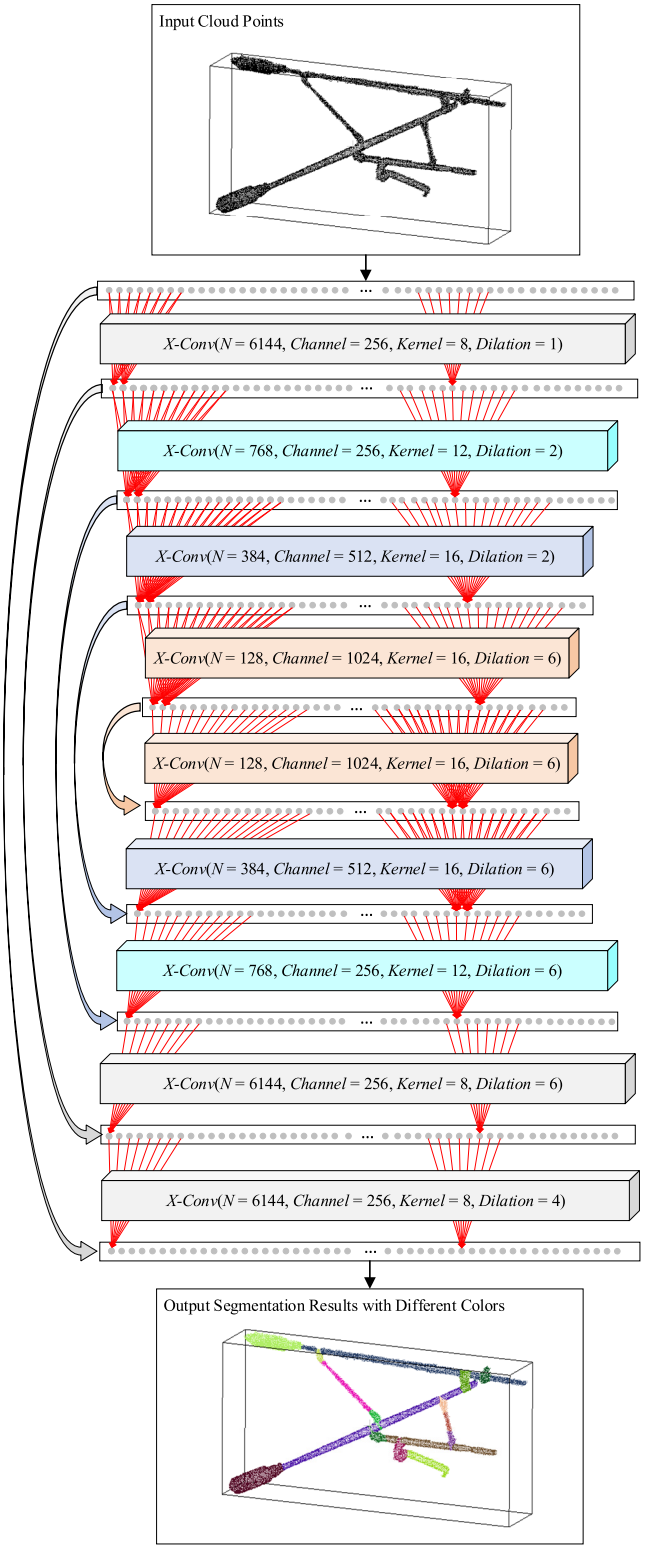

Fig. 6. Architecture of 3-D PointCNN based on the X-Conv operator.

and its dimensional is $C_2 = C_\delta + C_1$

$$\boldsymbol{f}_{2,j} = \left[\boldsymbol{f}^{\delta}_{2,j}, \boldsymbol{f}_{2,j}\right]. \tag{3}$$

Step 4 (Learn X-Transformation Matrix): Through the training and learning for the $\boldsymbol{P}$ sets of each point in p with an MLP,

Authorized licensed use limited to: TU Delft Library. Downloaded on January 13,2021 at 10:26:00 UTC from IEEE Xplore. Restrictions apply.

the $K \times K$ $\boldsymbol{X}$-transformation matrix is obtained

$$\boldsymbol{X} = MLP(\boldsymbol{P}'). \tag{4}$$

Step 5 (Weight and Permute Feature): When the transformation matrix and new features are obtained, the matrix $\boldsymbol{X}$ is used to weight and permutate the feature $\boldsymbol{f}_{2,j}$

$$\boldsymbol{F}_X = \boldsymbol{X} \times \boldsymbol{f}_{2,j}. \tag{5}$$

Step 6 (Feature Convolution): Lastly, the typical convolution operator is performed for the transformed feature $\boldsymbol{F}_X$ with kernel $\mathbf{K}$, and $\boldsymbol{F}_p$ is the convolution output

$$\boldsymbol{F}_p = \text{Conv}(\mathbf{K} \times \boldsymbol{F}_X). \tag{6}$$

2) Segmentation Architecture Based on X-Conv: In Fig. 6, the X-Conv-based 3-D PointCNN architecture is shown. First, the original catenary point clouds are uniformly sampled in 6144 points as the input data. Then, four X-Conv operators with different setting parameters are followed one by one. Next, for segmentation tasks, the high-resolution pointwise output is required, so this is realized by following the Conv-DeConv architecture and five DeConv operators. Note that both the Conv and DeConv are the X-Conv operators, and the only difference is that the latter has more points but fewer feature channels.

III. Cantilever Structure Parameter Measurement

To accurately measure the SPCCD, a fast and high-precision IP_RANSAC algorithm is proposed. First, the detection planes of cantilever device structures are divided to solve the occlusion problem. Next, the divided point cloud data are projected into the detected planes to extract the component axis with RANSAC. Lastly, SPCCD is calculated according to their spatial relationships.

A. Dividing Detection Plane of Cantilever Device Structures

Due to the occlusion interferences of different catenary cantilever devices in some special areas like catenary transition regions, we first use a fast RANSAC plane detection method. This method allows us to constraint the segmented component regions and accurately group each complete catenary cantilever device. Then, differently than the standard RANSAC, plane detection is performed by selecting three random points in the segmented local regions instead of global regions. Next, the steps are described:

Step 1 (Determine the First Detection Plane): First, calculating the detection plane and the distance from the point to the plane. As shown in Fig. 7, first, randomly sample three points P_1, P_2, P_3 from the point cloud set. Then, using the following equations, the detection plane and the point distance can be calculated. Different from the global random point selection method of the standard RANSAC [35], we randomly choose three points from the local segmented backbone component regions and calculate the plane parameters. As the plane is found in the segmented results instead of the point cloud data set, we expect a decrease in computing time and improve the detection efficiency as interference with other cloud points is avoided

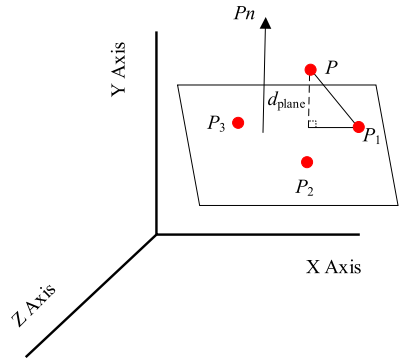

Fig. 7. Plane model detection with RANSAC.

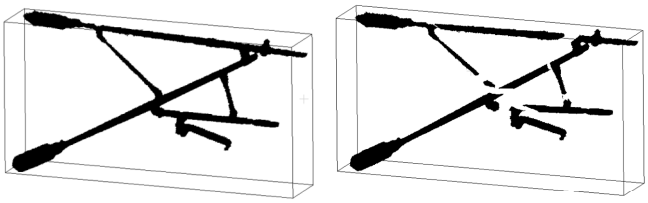

Fig. 8. Plane detection in catenary transition regions: (a) front detection plane and (b) back detection plane.

$$\overrightarrow{Pn} = \overrightarrow{P_2P_1} \times \overrightarrow{P_3P_1} \tag{7}$$

$$a(x - x_1) + b(y - y_1) + c(z - z_1) = 0 \tag{8}$$

$$d_{\text{plane}} = \frac{\overrightarrow{PP_1} \cdot \overrightarrow{Pn}}{\left\|\overrightarrow{Pn}\right\|} \tag{9}$$

where d_{plane} indicates the distance from the point to the detected plane, and the vector (a, b, c) is the normal of the plane.

Then, counting the number of inner points whose distance to the computed plane is smaller than the given distance threshold τ_{dp}, and iterating t_{dp} times to find and record the best plane, which includes most of the inner points.

Step 2 (Determine Other Detection Planes): Trim the point clouds of the detected plane and extract the next detection plane in the residual point clouds. Once the detected number of interior points is less than half of the remaining points, the plane detection process is terminated. As shown in Fig. 8, it is an example of plane detection in catenary transition regions.

B. Extracting Cantilever Backbone Component Axis

To calculate the SPCCD, we utilize a projection RANSAC straight-line detection method to extract the axis of the backbone components. Different from the projection RANSAC straight-line detection in [19], we project the point cloud data into the detection plane instead of the X–Y plane shown in Fig. 4(c), and the method can avoid the straight-line deviation caused by the point cloud being mapped back to

Authorized licensed use limited to: TU Delft Library. Downloaded on January 13,2021 at 10:26:00 UTC from IEEE Xplore. Restrictions apply.

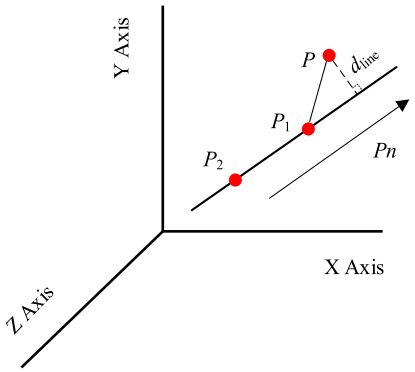

Fig. 9. Straight-line extraction with RANSAC.

the original space for the second time. The specific processes are the following.

Step 1 (Determine the First Backbone Component Axis): First, calculating the axis line of each segmented backbone component and the distance from the point to the line. As shown in Fig. 9, randomly sample two points P_1, P_2 from the point clouds set, and according to the following equations, the axis line of the segmented backbone component and the point distance can be calculated:

$$\overrightarrow{Ln} = \lambda \overrightarrow{P_2 P_1} \tag{10}$$

$$\frac{x - x_1}{l} = \frac{y - y_1}{m} = \frac{z - z_1}{n} \tag{11}$$

$$d_{\text{line}} = \frac{\left\| \overrightarrow{PP_1} \times \overrightarrow{Ln} \right\|}{\left\| \overrightarrow{Ln} \right\|} \tag{12}$$

where d_{line} is the distance from the point to the extracted axis, λ is a scale factor of the straight line, and (l, m, n) is the direction vector of the line.

Then, counting the number of inner points whose distance to the extracted axis line is smaller than a given distance threshold τ_{dl}, and iterating t_{dl} times to find and record the best line, which includes the most of the inner points.

Step 2 (Determine Another Component Axis): Repeat the above steps to find the next axis lines of cantilever backbone components until all the axis lines are detected. An example is shown in Fig. 10.

C. Detect the SPCCD

As shown in Fig. 11, when the axis line vector (l, m, n) of each backbone component is extracted, according to the backbone component connection relationship, the structure angle θ and the slope S of the steady arm can be calculated by the following equations. An example is shown in Fig. 12

$$\theta = \arccos \frac{\overrightarrow{(l_i, m_i, n_i)} \cdot \overrightarrow{(l_j, m_j, n_j)}}{\left| \overrightarrow{(l_i, m_i, n_i)} \right| \times \left| \overrightarrow{(l_j, m_j, n_j)} \right|} \tag{13}$$

$$S = \tan\left(\arccos \frac{\overrightarrow{(l_s, m_s, n_s)} \cdot \overrightarrow{(1, 0, 0)}}{\left| \overrightarrow{(l_s, m_s, n_s)} \right| \times \left| \overrightarrow{(1, 0, 0)} \right|}\right) \tag{14}$$

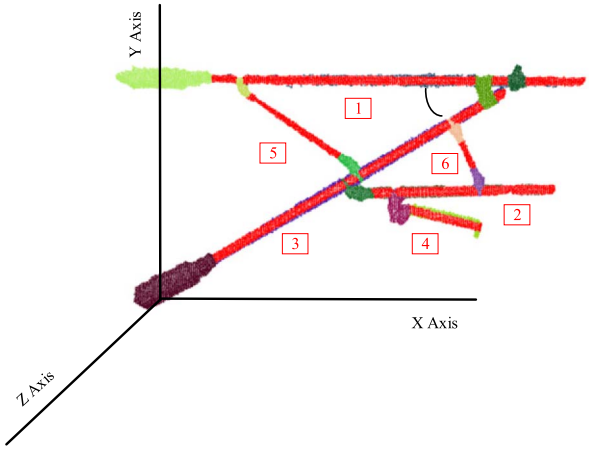

Fig. 10. Axis line extraction of catenary backbone components.

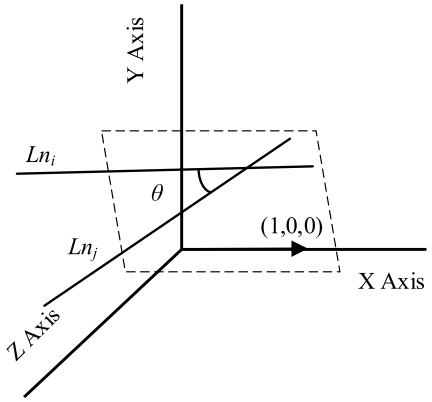

Fig. 11. Space angle calculation based on the spatial geometry calculation method.

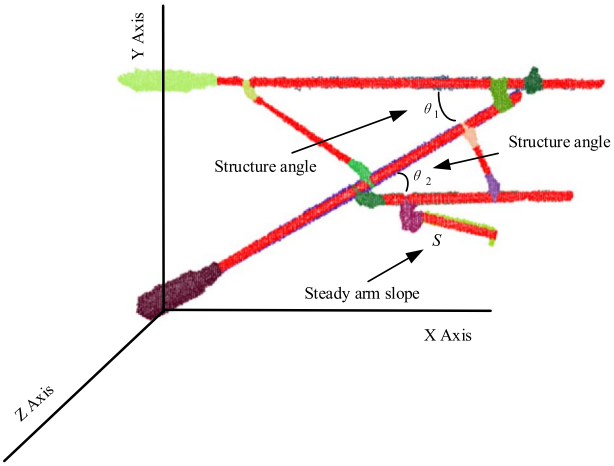

Fig. 12. SPCCDs.

where (l_i, m_i, n_i) and (l_j, m_j, n_j) denote the axis vectors of two backbone components. (l_s, m_s, n_s) is the axis vector of the steady arm component.

IV. Analysis and Discussion of Experimental Results

The performance of the proposed method is evaluated using a catenary image data set. All the experiments are conducted on a server with Intel (R) Xeon (R) CPU E5-2640 v4 at

Authorized licensed use limited to: TU Delft Library. Downloaded on January 13,2021 at 10:26:00 UTC from IEEE Xplore. Restrictions apply.

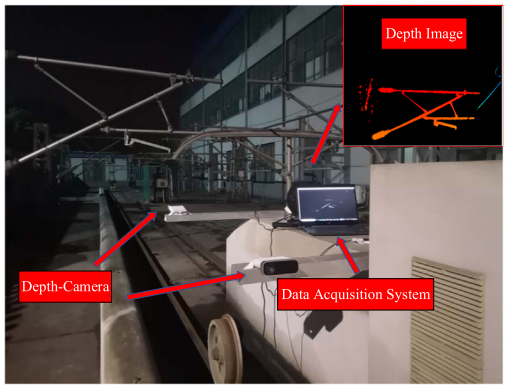

Fig. 13. 3-D data acquisition system in the field.

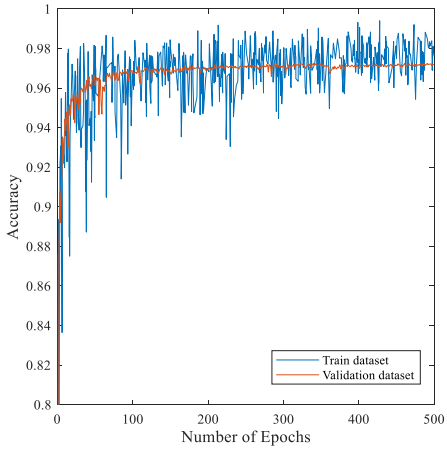

Fig. 14. Segmentation accuracy of catenary point clouds for the training and validation data set during the training phase.

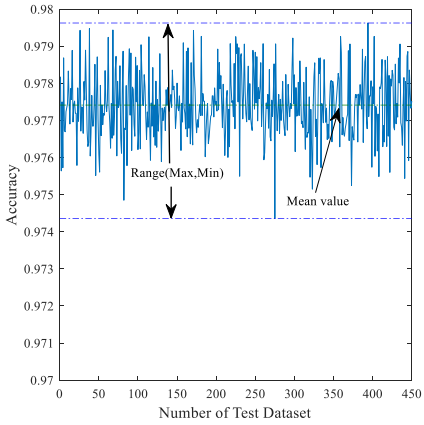

Fig. 15. Segmentation accuracy of catenary point clouds for the test data set during the testing phase.

2.40 GHz, TITAN RTX 24G GPU, 32-GB RAM, and 2-TB SSD. All core algorithm codes are developed with TensorFlow architecture [36] and MATLABon Linux 18.04 system.

A. Component Segmentation

1) Data Set: As shown in Fig. 13, the catenary 3-D point cloud data are acquired from the Azure Kinect sensor camera installed on the beam on the top of the inspection vehicle. The camera is a 100-million-pixel time-of-flight (TOF) depth scanner and complies with all characteristics of the image sensor presented in ISSCC 2018 [37]. The working range is from 0.5 to 5.46 m. The field of view (FOV) can cover 75 × 65°. The sensor camera can work well under the following conditions: temperature between 10 °C and 25 °C, humidity between 8% and 90% with noncondensing relative humidity, and low natural light interference environment (<3 klux). To accurately segment the parts, we fuse 20 frames of point cloud data taken continuously the same location into a set of data to fill the holes due to uneven reflection, ensuring that the deviation between data is as small as possible and improving the performance of the proposed method. The total amount of cantilever devices point cloud data set is 3000, among which the training data are 2000, the validation data are 550, and the test data are 450. And the 3-D point cloud labeling is achieved based on the open-source code (https://github.com/cloudcompare/cloudcompare).

2) Model Parameters: The 3-D PointCNN parameters are initialized with the pretrained parameters on a benchmark data set. The Momentum algorithm is chosen as the backpropagation gradient descent method, and the term momentum and weight decay are set to 0.9 and 0.0001, respectively. The learning rate is 0.0001, and the max iteration epoch is 500.

3) Evaluation Indexes: To evaluate the performance of the 3-D PointCNN, the metric point ratio P_R is used to validate the accuracy of segmentation. The average error $\text{Error}_{\text{average}}$ is calculated to evaluate the robustness of the solution

$$P\_R = \sum_{i=1}^{K} \text{TP}_i \Big/ \sum_{i=1}^{K} N_i \times 100\% \tag{15}$$

$$\text{Error}_{\text{average}} = \frac{1}{M} \sum_{j=1}^{M} (100\% - P\_R_j) \tag{16}$$

where TP_i donates the predicted point number of the true positive in category i, N_i indicates the total point number of categories i, and K is the number of component categories. M is the sample number of the test data set of catenary cantilever devices.

4) Experimental Results and Analysis:

1) Fig. 14 shows the training process of the 3-D PointCNN for the catenary cantilever segmentation. The segmentation accuracy for the training and validation data set begins to converge about 97% after 200 epochs, respectively. These curves fluctuate smoothly. These results demonstrate that the trained model has high accuracy and strong robustness.
2) Fig. 15 and Table I indicate the segmentation accuracy of the trained model for the testing data set. The adopted 3-D PointCNN can precisely segment catenary cantilever 3-D point cloud data, and the accuracy can achieve 97.7% on average. By comparing and analyzing with the results of [19], as shown in Table I, we can see that both the average error range 1.3%–2.6% and the average error 2.2% are lower than the results in [19]. These results show the accuracy and stability of our method.

Authorized licensed use limited to: TU Delft Library. Downloaded on January 13,2021 at 10:26:00 UTC from IEEE Xplore. Restrictions apply.

TABLE I
STATISTICS OF THE AVERAGE ERROR OF THE TESTING DATA SET

Method	Average Error range	Average Error
SC_LCCP [19]	2.3%-5.3%	3.80%
3D PointCNN (this paper)	2.0%-2.3%	2.26%

TABLE II
PLANE DETECTION WITH DIFFERENT METHODS

Methods	Detection Speed/ms
Global RANSAC	2.83
Local RANSAC (this paper)	2.12

3) Through statistical analysis of the computational load with the two methods on our test data set, the average computational load of our segmentation method is 0.48 frames/s, and the average computational load of the method in [19] is 0.04 frames/s. Obviously, our algorithm takes more time due to the model, but the basic real-time performance can still be guaranteed.

B. Plane Extraction

1) Model Parameters and Evaluation Indexes: To extract all detection planes of each catenary cantilever device on the same pillar, we utilized: 1) the ratio IP_R between the number N_{inc} of those points included in the extracted plane in the distance threshold τ_{dp} and 2) the total number N_{tot} of those backbone components as an indicator to choose the optimal model parameter and evaluate the accuracy of the extracted detection plane. Here, in order to ensure that the plane is accurately detected, the iteration t_{dp} is set into 1000. Besides, to prove the performance of the improved local RANSAC, we do a comparative experiment, including the detection accuracy and detection speed, as shown in Fig. 12 and Table II

$$\text{IP\_}R = \frac{N_{\text{inc}}}{N_{\text{tot}}} \tag{17}$$

2) Experimental Results and Analysis:

1) Fig. 16 shows that the detection accuracy of the local RANSAC proposed can achieve 96.5% around the distance threshold 0.035 m, while the accuracy of the global RANSAC is 81.1%. According to the actual radius of catenary cantilever backbone components, the radius range is between about 0.02 and 0.04 m, and the parameter of the proposed local RANSAC matches this range. This also indicates that the proposed approach can more exactly and completely extract the detection plane.
2) Table II shows that the detection speed of the local RANSAC is 0.71 ms faster than the global RANSAC. Thus, the proposed method is faster by searching planes in local segmented points rather than global points while ensuring the detection accuracy.

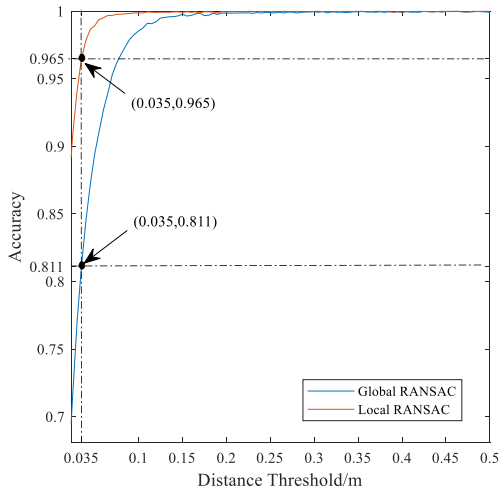

Fig. 16. Plane extraction accuracy with different methods.

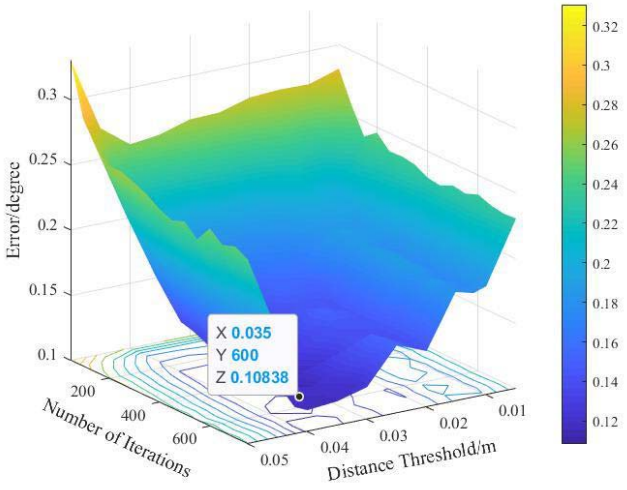

Fig. 17. Axis line errors in different model parameters.

C. Axis Line Detection of Cantilever Backbone Components

1) Model Parameters and Evaluation Indexes: To evaluate the performance of the proposed method IP_RANSAC for detecting the axis line of cantilever backbone components, we calculate the angle β between the detected axis line and X-axis and compare with their real angle β_{ij}^{real} those are manually extracted. Through the index of the angle error, the effectiveness of the proposed method can be proved. To choose the optimal parameters of the model, including the distance threshold τ_{dl} and the iteration time t_{dl}, a set of experiments is developed to determine them by measuring the index of the angle error, as shown in Fig. 16

$$\beta = \arccos \frac{\overrightarrow{(l,m,n)} \cdot \overrightarrow{(0,0,1)}}{\left|\overrightarrow{(l,m,n)}\right| \times \left|\overrightarrow{(0,0,1)}\right|} \tag{18}$$

$$\text{Error}_{\beta} = \frac{1}{NM} \sum_{i=1}^{N} \sum_{j=1}^{M} \left| \beta_{ij} - \beta_{ij}^{\text{real}} \right|. \tag{19}$$

2) Experimental Results and Analysis: From Fig. 17, we can see that the angle error of the model is minimal when

Authorized licensed use limited to: TU Delft Library. Downloaded on January 13,2021 at 10:26:00 UTC from IEEE Xplore. Restrictions apply.

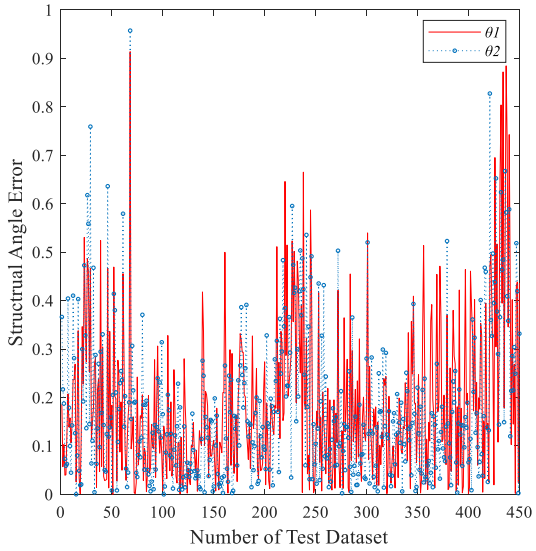

(a)

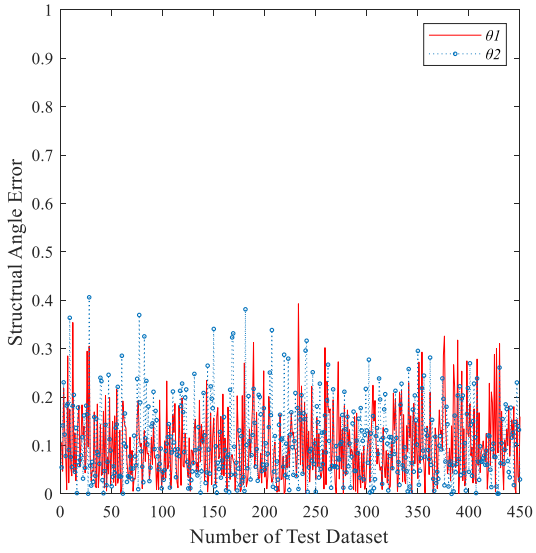

(b)

Fig. 18. Structural angle errors in different methods: (a) is the results with the method [19] and (b) denotes the results with our proposed method.

TABLE III
STATISTICS OF THE STRUCTURAL ANGLE ERRORS

Indexes	Mean value	Standard deviation
P_RANSAC [19]	0.1790°	0.1567°
IP_RANSAC (this paper)	0.1029°	0.0773°

the distance threshold is 0.035 m, and the iteration time is 600. As mentioned above, the radius range of backbone components is between 0.02 and 0.04 m, and their average radius is near 0.035 m, which also indirectly demonstrates the rationality and effectiveness of parameter selection. Furthermore, the minimal angle error is 0.1084°, which shows that the proposed approach has very high precision.

D. Parameter Detection

1) Evaluation Indexes: The effectiveness of the proposed parameter detection method is evaluated with the errors

TABLE IV
STATISTICS OF THE SLOPE ERRORS

Indexes	Mean value	Standard deviation
P_RANSAC [19]	1.63%	1.73%
IP_RANSAC (this paper)	1.19%	0.99%

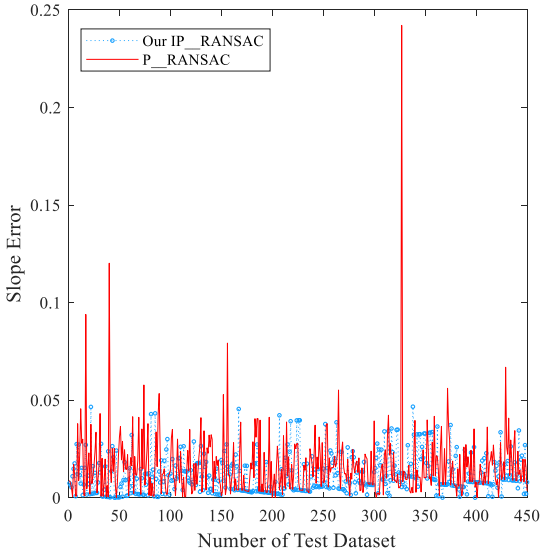

Fig. 19. Slope errors in different methods.

$\text{Error}_{\theta_{\text{str}}}$ and $\text{Error}_{S_{\text{std}}}$ of the structural angle of catenary cantilevers and the slope of steady arms between their calculated values θ^i_{str}, S^i_{std} and true values $\theta^i_{\text{str\_tru}}$, $S^i_{\text{std\_true}}$. True values were measured manually to certify the accuracy of the proposed method. Moreover, the expectation and variance of the errors are calculated to show the stability of the proposed method. Also, the results are compared with the method in [19] on our data set, and the results are shown in Figs. 18 and 19, and Tables III and IV

$$\text{Error}_{\theta_{\text{str}}} = \left|\theta^i_{\text{str}} - \theta^i_{\text{str\_tru}}\right|, \quad i = 1 \ldots N \tag{20}$$

$$\text{Error}^{\text{exp}}_{\theta_{\text{str}}} = \frac{1}{N}\sum_{i=1}^{N} \text{Error}_{\theta_{\text{str}}} \tag{21}$$

$$\text{Error}^{\text{var}}_{\theta_{\text{str}}} = \sqrt{\frac{\sum_{i=1}^{N}\left|\text{Error}^i_{\theta_{\text{str}}} - \text{Error}^{\text{exp}}_{\theta_{\text{str}}}\right|}{N}} \tag{22}$$

$$\text{Error}_{S_{\text{std}}} = \left|S^i_{\text{std}} - S^i_{\text{std\_true}}\right| / S^i_{\text{std\_real}}, i, \ldots, N \tag{23}$$

$$\text{Error}^{\text{exp}}_{S_{\text{std}}} = \frac{1}{N}\sum_{i=1}^{N} \text{Error}^i_{S_{\text{std}}} \tag{24}$$

$$\text{Error}^{\text{var}}_{S_{\text{std}}} = \sqrt{\frac{\sum_{i=1}^{N}\left|\text{Error}^i_{S_{\text{std}}} - \text{Error}^{\text{exp}}_{S_{\text{std}}}\right|}{N}}. \tag{25}$$

2) Experimental Results and Analysis:

1) From Fig. 18 and Table III, the structural angle error of the proposed method is 0.1029°, and it is lower than the errors with the method in [19] by 0.0761°. Besides, the proposed method has a smaller variance, so the method is more stable.

Authorized licensed use limited to: TU Delft Library. Downloaded on January 13,2021 at 10:26:00 UTC from IEEE Xplore. Restrictions apply.

2) In Fig. 19 and Table IV, it shows that the slope error of the proposed method is 1.19% and lower than the errors with the method in [19] by 0.44%. Also, the proposed method has a smaller variance, which denotes the method is more stable. The detection precision of the slope parameter is very high and can fully meet the detection requirement in the field.

E. Discussion

Through the analysis of experiment results, the proposed method can successfully solve the occlusion interference problem of two cantilever devices on the pillar. Furthermore, the proposed method has higher parameter detection accuracy. However, in some areas of more complicated railway lines, there may be three or more cantilever devices on the pillar, and the internal devices cannot be accurately detected. There are no better solutions and methods in the current research, and further research is needed.

V. Conclusion

This article proposed a method for structure parameter detection of catenary cantilevers using 3-D cloud data measurements. The major features of the method are as follows.

1) The segmentation and recognition methods are based on 3-D CNN to segment catenary cantilever devices. The method does not require complex tuning procedures of a large set of parameters as in conventional methods and ensures the feasibility of the defect detection method.
2) The improved projection RANSAC method successfully solves the occlusion interferences of different catenary cantilever devices in catenary transition regions. It can avoid the straight-line deviation caused by the point cloud being mapped back to the original space for the second time and improve the accuracy of SPCCD measurement.

The proposed SPCCD detection method obtains high accuracy detection. Thus, the method will allow the practical implementation of 3-D point cloud data measurements and automatic detection in the railway infrastructure. Further research includes accuracy improvement using sophisticated calibration methods. Other further research lines include: 1) a comparison with a broader range of segmentation methods, including those from a classical point of view, 2) robustness improvement by augmenting more different railway line data, 3) the analysis of defect diagnosis technology through multichannel data, and 4) the fusion of the characteristics of catenary 2-D images and 3-D point cloud data via multimodal DL techniques together with dynamic measurements.

References

[1] J. Chen, Z. Liu, H. Wang, A. Nunez, and Z. Han, "Automatic defect detection of fasteners on the catenary support device using deep convolutional neural network," *IEEE Trans. Instrum. Meas.*, vol. 67, no. 2, pp. 257–269, Feb. 2018.

[2] W. Liu *et al.*, "Multi-objective performance evaluation of the detection of catenary support components using DCNNs," *IFAC-PapersOnLine*, vol. 51, no. 9, pp. 98–105, 2018.

[3] Y. Song, Z. Liu, A. Rønnquist, P. Nåvik, and Z. Liu, "Contact wire irregularity stochastics and effect on high-speed railway pantograph-catenary interactions," *IEEE Trans. Instrum. Meas.*, vol. 69, no. 10, pp. 8196–8206, Oct. 2020.

[4] Z. Liu, L. Wang, C. Li, and Z. Han, "A high-precision loose strands diagnosis approach for isoelectric line in high-speed railway," *IEEE Trans. Ind. Informat.*, vol. 14, no. 3, pp. 1067–1077, Mar. 2018.

[5] W. Liu, Z. Liu, H. Wang, and Z. Han, "An automated defect detection approach for catenary rod-insulator textured surfaces using unsupervised learning," *IEEE Trans. Instrum. Meas.*, vol. 69, no. 10, pp. 8411–8423, Oct. 2020, doi: 10.1109/TIM.2020.2987503.

[6] G. K. Deep, S. Gao, L. Yu, and D. Zhang, "Architecture for high-speed railway insulator surface defect detection: Denoising autoencoder with multitask learning," *IEEE Trans. Instrum. Meas.*, vol. 68, no. 8, pp. 2679–2690, Aug. 2020.

[7] J. Zhong, Z. Liu, Z. Han, Y. Han, and W. Zhang, "A CNN-based defect inspection method for catenary split pins in high-speed railway," *IEEE Trans. Instrum. Meas.*, vol. 68, no. 8, pp. 2849–2860, Aug. 2019.

[8] Z. Liu, K. Liu, J. Zhong, Z. Han, and W. Zhang, "A high-precision positioning approach for catenary support components with multiscale difference," *IEEE Trans. Instrum. Meas.*, vol. 69, no. 3, pp. 700–711, Mar. 2020, doi: 10.1109/TIM.2019.2905905.

[9] W. Liu, Z. Liu, A. Núñez, and Z. Han, "Unified deep learning architecture for the detection of all catenary support components," *IEEE Access*, vol. 8, pp. 17049–17059, 2020.

[10] H. Yin, Z. Liu, Z. Xu, and L. Gao, "An automatic visual monitoring system for expansion displacement of switch rail," *IEEE Trans. Instrum. Meas.*, vol. 69, no. 6, pp. 3015–3025, Jun. 2020.

[11] C. J. Cho and H. Ko, "Video-based dynamic stagger measurement of railway overhead power lines using rotation-invariant feature matching," *IEEE Trans. Intell. Transp. Syst.*, vol. 16, no. 3, pp. 1294–1304, Jun. 2015.

[12] Z. Liu, W. Liu, and Z. Han, "A high-precision detection approach for catenary geometry parameters of electrical railway," *IEEE Trans. Instrum. Meas.*, vol. 66, no. 7, pp. 1798–1808, Jul. 2017.

[13] D. Zhan, D. Jing, M. Wu, D. Zhang, L. Yu, and T. Chen, "An accurate and efficient vision measurement approach for railway catenary geometry parameters," *IEEE Trans. Instrum. Meas.*, vol. 67, no. 12, pp. 2841–2853, Dec. 2018.

[14] Y. Yang, W. Zhang, Z. He, and D. Chen, "Locator slope calculation via deep representations based on monocular vision," *Neural Comput. Appl.*, vol. 31, no. 7, pp. 2781–2794, Jul. 2019.

[15] B. Q. Guo, Z. J. Yu, N. Zhang, L. Zhu, and C. Gao, "3D point cloud segmentation classification and recognition algorithm of railway scene," *Chin. J. Sci. Instrum.*, vol. 38, no. 9, pp. 2103–2111, 2017.

[16] G. Gabara and P. Sawicki, "A new approach for inspection of selected geometric parameters of a railway track using image-based point clouds," *Sensors*, vol. 18, no. 3, p. 791, Mar. 2018.

[17] J. Zhou, Z. Han, and C. Yang, "Catenary geometric parameters detection method based on 3D point cloud," *Chin. J. Sci. Instrum.*, vol. 39, no. 4, pp. 239–246, Apr. 2018.

[18] W. Liu, Z. Liu, and A. Nunez, "Virtual reality and convolutional neural networks for railway catenary support components monitoring," in *Proc. IEEE Intell. Transp. Syst. Conf. (ITSC)*, Oct. 2019, pp. 2183–2188.

[19] Z. Han, C. Yang, and Z. Liu, "Cantilever structure segmentation and parameters detection based on concavity and convexity of 3-D point clouds," *IEEE Trans. Instrum. Meas.*, vol. 69, no. 6, pp. 3026–3036, Jun. 2020, doi: 10.1109/TIM.2019.2930158.

[20] J. Papon, A. Abramov, M. Schoeler, and F. Wörgötter, "Voxel cloud connectivity segmentation—Supervoxels for point clouds," in *Proc. IEEE Comput. Vis. Pattern Recognit.*, vol. 9, Jun. 2013, pp. 2027–2034.

[21] S. C. Stein, M. Schoeler, and J. Papon, "Wörgötter, Object partitioning using local convexity," in *Proc. IEEE Comput. Vis. Pattern Recognit.*, Jun. 2014, pp. 304–311.

[22] R. Schnabel, R. Wahl, and R. Klein, "Efficient RANSAC for point-cloud shape detection," in *Computer Graphics Forum*, vol. 26, no. 2. Oxford, U.K.: Blackwell, Jun. 2007, pp. 214–226.

[23] H. He, S. Jin, C.-K. Wen, F. Gao, G. Y. Li, and Z. Xu, "Model-driven deep learning for physical layer communications," *IEEE Wireless Commun.*, vol. 26, no. 5, pp. 77–83, Oct. 2019.

[24] S. Ravanbakhsh, J. Schneider, and B. Poczos, "Deep learning with sets and point clouds," 2016, *arXiv:1611.04500*. [Online]. Available: http://arxiv.org/abs/1611.04500

[25] M. Zaheer, S. Kottur, S. Ravanbakhsh, B. Poczos, R. R. Salakhutdinov, and A. J. Smola, "Deep sets," in *Proc. Adv. Neural Inf. Process. Syst.*, 2017, pp. 3391–3401.

Authorized licensed use limited to: TU Delft Library. Downloaded on January 13,2021 at 10:26:00 UTC from IEEE Xplore. Restrictions apply.

[26] C. R. Qi, L. Yi, H. Su, and L. J. Guibas, "Pointnet++: Deep hierarchical feature learning on point sets in a metric space," in *Proc. Adv. Neural Inf. Process. Syst.*, 2017, pp. 5099–5108.
[27] J. Li, B. M. Chen, and G. Hee Lee, "So-net: Self-organizing network for point cloud analysis," in *Proc. IEEE Conf. Comput. Vis. Pattern Recognit.*, Jun. 2018, pp. 9397–9406.
[28] Y. Shen, C. Feng, Y. Yang, and D. Tian, "Mining point cloud local structures by kernel correlation and graph pooling," in *Proc. IEEE Conf. Comput. Vis. Pattern Recognit.*, Jun. 2018, pp. 4548–4557.
[29] H. Su, V. Jampani, D. Sun, S. Maji, E. Kalogerakis, M. H. Yang, and J. Kautz, "SPLATNet: Sparse lattice networks for point cloud processing," in *Proc. IEEE Conf. Comput. Vis. Pattern Recognit.*, Jun. 2018, pp. 2530–2539.
[30] M. Tatarchenko, J. Park, V. Koltun, and Q.-Y. Zhou, "Tangent convolutions for dense prediction in 3D," in *Proc. IEEE/CVF Conf. Comput. Vis. Pattern Recognit.*, Jun. 2018, pp. 3887–3896.
[31] F. Groh, P. Wieschollek, and H. P. A. Lensch, "Flex-convolution (million-scale point-cloud learning beyond grid-worlds)," 2018, *arXiv:1803.07289*. [Online]. Available: http://arxiv.org/abs/1803.07289
[32] S. Wang, S. Suo, W.-C. Ma, A. Pokrovsky, and R. Urtasun, "Deep parametric continuous convolutional neural networks," in *Proc. IEEE/CVF Conf. Comput. Vis. Pattern Recognit.*, Jun. 2018, pp. 2589–2597.
[33] Y. Xu, T. Fan, M. Xu, L. Zeng, and Y. Qiao, "SpiderCNN: Deep learning on point sets with parameterized convolutional filters," in *Proc. Eur. Conf. Comput. Vis. (ECCV)*, Sep. 2018 pp. 87–102.
[34] Y. Li, R. Bu, M. Sun, W. Wu, X. Di, and B. Chen, "PointCNN: Convolution on $\mathcal{X}$-transformed points," 2018, *arXiv:1801.07791*. [Online]. Available: http://arxiv.org/abs/1801.07791
[35] M. Y. Yang and W. Förstner, "Plane detection in point cloud data," in *Proc. Int. Conf. Mach. Control Guid.*, Jan. 2010, pp. 95–104.
[36] M. Abadi *et al.*, "TensorFlow: Large-scale machine learning on heterogeneous distributed systems," 2016, *arXiv:1603.04467*. [Online]. Available: http://arxiv.org/abs/1603.04467
[37] C. S. Bamji, "IMpixel 65 nm BSI 320 MHz demodulated TOF Image sensor with 3μm global shutter pixels and analog binning," in *IEEE Int. Solid-State Circuits Conf. (ISSCC) Dig. Tech. Papers*, Feb. 2018, pp. 94–96.

Wenqiang Liu (Graduate Student Member, IEEE) received the B.S. degree in electronic information engineering from Southwest Jiaotong University, Chengdu, China, in 2013, where he is currently pursuing the Ph.D. degree with the School of Electrical Engineering.

His current research interests include image processing, computer vision, deep learning, reinforcement learning, 3-D modeling, and virtual reality and their applications in fault detection and diagnosis in the electrified railway industry.

Zhigang Liu (Senior Member, IEEE) received the Ph.D. degree in power system and its automation from Southwest Jiaotong University, Chengdu, China, in 2003.

He is currently a Full Professor with the School of Electrical Engineering, Southwest Jiaotong University. His research interests include the electrical relationship of EMUs and traction, detection, and assessment of pantograph-catenary in high-speed railway. He has written three books and published more than 100 peer-reviewed journal and conference papers.

Dr. Liu was elected as a fellow of The Institution of Engineering and Technology (IET) in 2017. He is an Associate Editor of the IEEE TRANSACTIONS ON NEURAL NETWORKS AND LEARNING SYSTEMS, IEEE TRANSACTIONS ON VEHICULAR TECHNOLOGY, IEEE TRANSACTIONS ON INSTRUMENTATION AND MEASUREMENT, and IEEE ACCESS. He received the IEEE TRANSACTIONS ON INSTRUMENTATION AND MEASUREMENT's Outstanding Associate Editors for 2019 as well as the Outstanding Reviewer of the IEEE TRANSACTIONS ON INSTRUMENTATION AND MEASUREMENT for 2018.

Qiao Li (Graduate Student Member, IEEE) received the B.S. degree in the electrical engineering and automation from the School of Automation Science and Electrical Engineering, Lanzhou Jiaotong University, Lanzhou, China, in 2018. He is currently pursuing the M.S. degree with the College of Electrical Engineering, Southwest Jiaotong University, Chengdu, China.

His current research interests include 2-D image processing, 3-D point cloud deep learning, semantic segmentation, and their applications in the electrified railway industry.

Zhiwei Han (Member, IEEE) received the Ph.D. degree in power system and its automation from Southwest Jiaotong University, Chengdu, China, in 2013.

He is currently a Lecturer with the School of Electrical Engineering, Southwest Jiaotong University. His current research interests include modern signal processing and computer vision and their application in railway and electric power system

Alfredo Núñez (Senior Member, IEEE) received the Ph.D. degree in electrical engineering from the Universidad de Chile, Santiago, Chile, in 2010.

He was a Post-Doctoral Researcher with the Delft Center for Systems and Control, Delft, The Netherlands. Since 2013, he has been with the Section of Railway Engineering, Department of Engineering Structures, Delft University of Technology, Delft, where he is currently an Assistant Professor in the topic data-based maintenance for railway infrastructure. His current research interests include the maintenance of railway infrastructures, intelligent conditioning monitoring in railway systems, big data, risk analysis, and optimization.

Dr. Núñez is on the Editorial Board of the journal *Applied Soft Computing*, Elsevier. He is an Associate Editor of the journal IEEE TRANSACTIONS ON INTELLIGENT TRANSPORTATION SYSTEMS.

Authorized licensed use limited to: TU Delft Library. Downloaded on January 13,2021 at 10:26:00 UTC from IEEE Xplore. Restrictions apply.